

Correlation of Magnetism and Disordered Shiba bands in Fe Monolayer Islands on Nb(110)

Julia J. Goedecke,^{*,†} Lucas Schneider,[†] Yingqiao Ma,^{†,‡} Khai Ton That,[†]
Dongfei Wang,^{†,¶} Jens Wiebe,^{*,†} and Roland Wiesendanger[†]

[†]*Department of Physics, University of Hamburg, D-20355 Hamburg, Germany*

[‡]*Present address: Beijing National Laboratory for Molecular Sciences, CAS Key Laboratory of Organic Solids, Institute of Chemistry, Chinese Academy of Sciences, Beijing 100190, China*

[¶]*Present address: CIC Nanogune, Tolosa Hiribidea, 76 E-20018 Donostia – San Sebastian*

E-mail: julia.goedecke@physnet.uni-hamburg.de; jwiebe@physnet.uni-hamburg.de

Abstract

Two-dimensional (2D) magnet-superconductor hybrid systems are intensively studied due to their potential for the realization of 2D topological superconductors with Majorana edge modes. It is theoretically predicted that this quantum state is ubiquitous in spin-orbit coupled ferromagnetic or skyrmionic 2D spin-lattices in proximity to an *s*-wave superconductor. However, recent examples suggest that the requirements for topological superconductivity are complicated by the multi-orbital nature of the magnetic components and disorder effects. Here, we investigate Fe monolayer islands grown on a surface of the *s*-wave superconductor with the largest gap of all elemental superconductors, Nb, with respect to magnetism and superconductivity using spin-resolved

scanning tunneling spectroscopy. We find three types of Fe monolayer islands which differ by their reconstruction inducing disorder, the magnetism and the sub-gap electronic states. All three types are ferromagnetic with different coercive fields indicating diverse exchange and anisotropy energies. On all three islands, there is finite spectral weight throughout the substrate's energy gap at the expense of the coherence peak intensity, indicating the formation of Shiba bands overlapping with the Fermi energy. The gap filling and coherence peak reduction is strongest for the island with largest coercive field. A strong lateral variation of the spectral weight of the Shiba bands signifies substantial disorder on the order of the substrate's pairing energy with a length scale of the period of the three different reconstructions. There are neither signs of topological gaps within these bands nor of any kind of edge modes. Our work illustrates that a reconstructed growth mode of magnetic layers on superconducting surfaces is detrimental for the formation of 2D topological superconductivity.

Introduction

Two-dimensional (2D) chiral p -wave, or more generally *topological*, superconductors are predicted to host exotic dispersive 1D electron states on their edges, named Majorana edge modes.¹ Such systems recently attracted a lot of attention because of their potential for the realization of concepts for fault tolerant quantum computation.² One of the most prominent proposals for the realization of such topological superconductors are Shiba-lattices, i.e. 2D lattices of magnetic atoms, or thin magnetic layers, deposited on the surface of a conventional s -wave superconductor which supplies strong spin-orbit coupling.³⁻⁶ Related concepts which eliminate the need of strong spin-orbit coupling⁷ propose the utilization of non-collinear spin structures,⁷⁻⁹ in particular Skyrmions¹⁰⁻¹³ or Skyrmion-like spin-structures¹⁴ coupled to conventional s -wave superconductors.

Experimental investigations of 2D Shiba-lattices so far focused on magnetic transition metal islands on superconducting crystals with a thin oxide decoupling layer,¹⁵ van-der-Waals

heterostructures,^{16,17} transition metal-silicon alloys buried below superconducting layers,^{18,19} spin-spirals²⁰ or antiferromagnetic transition metal layers on elemental superconductors.²¹ The reported experimental evidences of topological superconductivity in some of these systems^{15–19} relied on the detection of zero bias resonances or an enhanced density of states localized on the rim of the lattice. However, it was theoretically predicted that the Majorana edge modes have a dispersion, which can be experimentally resolved.²² The realization of Shiba-lattices directly on a surface of a metal usually enables atomic manipulation^{23,24} and, thereby, would permit the building of more complex structures, as, e.g. 1D Shiba-chains attached to 2D Shiba-lattices allowing for additional experiments in order to prove or disprove the Majorana edge mode origin of enhanced densities of states.²⁵

Yet, studies of transition metal layers in *direct* contact to elementary superconductors did not show indications for topological superconductivity and dispersing Majorana edge modes.¹⁵ For such lattices in direct contact to the superconductor, the realization of a SC state in the ferromagnet by the proximity effect^{26–28} can be hampered by a strong inverse proximity effect, which may reduce the magnetism^{29,30} and might also quench the superconductivity in the vicinity of the Shiba-lattice (see citations in²⁸). Another important issue for the development of 2D topological superconductivity is disorder. It has been shown theoretically, that disorder can have strong effects on the topologically superconducting properties of 1D^{31–34} and 2D^{35–37} Shiba-lattices. Considering potential disorder in the superconductor, it has been shown for the case of a ferromagnetic spin chain (1D),³⁴ that the topological minigap is very sensitive to disorder, but the MM is surprisingly insensitive, as long as the surrounding superconductor does not show signs of strong disorder. For the 2D case, e.g. induced in a layer with a Rashba-type spin-orbit coupling sandwiched between a ferromagnet and a superconductor,³⁶ very weak potential disorder first decreases the Majorana bound state localization length with increasing disorder strength. However, it increases again when the disorder gets on the order of the pairing energy. This sensitivity can get even stronger for correlated disorder³⁷ and is particularly effective if the correlation length of the disorder

in the chemical potential is comparable with the coherence length of the superconductor. Magnetic disorder was investigated for the 1D spin-chain system, e.g. induced by missing magnetic atoms or variations in the Shiba couplings,³³ and showed that the topological phase is relatively sensitive to such kinds of disorder. For the 2D system,³⁵ magnetic disorder either in the form of a disordered magnetic coupling between a ferromagnetic lattice and the electrons in the superconductor, for randomly oriented spins, or for randomly missing spins, more strongly suppresses the topological phases as compared to potential disorder. Here, the latter type of magnetic disorder leads to the strongest suppression of topological phases, but correlated disorder has a weaker effect. On the other hand, magnetic disorder may also favor topological phases in 2D Shiba-lattices, e.g. for very particular values of the chemical potential,³⁵ for Moiré-lattices,¹⁷ or for a spin-glass state.³⁸ Therefore, it is surprising, that disorder effects in 1D^{39,40} or 2D Shiba-lattices¹⁷⁻¹⁹ have been barely touched on experimentally.

Here, we experimentally investigate ferromagnetic 2D Shiba-lattices of the transition metal Fe grown directly ontop of the clean (110) surface of Nb, the elemental superconductor with the largest energy gap. We find that the system realizes strongly disordered Shiba-bands induced by ferromagnetic Fe monolayer reconstructions, and study these bands with respect to indications for topological superconductivity.

Results and Discussion

Reconstructions of the Fe monolayer grown on clean Nb(110)

The growth of Fe on the (110) surface of Nb films deposited on various substrates has previously been intensely studied by RHEED, Auger-electron spectroscopy, LEED and STM.^{41,42} For room temperature deposition of very thin Fe films, which is also the case studied in the current work, there are no signs of intermixing between Fe and Nb.^{41,42} Here, we grow thin films of Fe on the clean oxygen-reconstruction-free (110) surface of a Nb single crystal (Figure 1a,b) which is achieved by carefully flashing the crystal in ultra-high vacuum to

very high temperatures (see Methods). Note, that for previous studies, the substrate most probably was still at least partly oxygen-reconstructed resulting in a different Fe structure compared to the results we present here (see Supplementary Note 1 and Figure S1). After RT evaporation of Fe with less than a monolayer (ML) coverage onto such clean Nb(110) surfaces, three different reconstructions were observed on ML Fe islands (see Figure 1a) with a typical height of 250 pm (Figures 3 and 4d below), referred to as type I, II and III in the following. In addition, a few double-layered (DL) Fe islands (bright stripe) can be found, which are elongated along the [001]-direction. All three Fe ML reconstructions are found within single islands but also on separate islands. Figures 1b-e show atomically resolved STM images of the Nb(110) substrate and of the individual reconstructions. In the following, we will always use the same color code in order to indicate the different types of reconstruction in the Figures: blue for type I, orange for type II, and green for type III. In Figure 1b, the atomic lattice of Nb(110) is visible and the surface unit cell is marked. For comparison, this unit cell is added to the STM images of the three Fe ML reconstructions in Figures 1c-e. The reconstructions I and III span a large number of substrate unit cells. Type I (Figure 1c) consists of 1 to 2 nm long stripes with a larger apparent height arranged on a roughly 8×16 superlattice (with respect to $[001] \times [1\bar{1}0]$) separated by rather flat areas. Type III (Figure 1e) consists of units that span 4×3 to 7×4 unit cells interrupted by dislocation lines along [001]. The arrangements of both of these reconstructions are strongly influenced by the island's shape. Reconstruction II spans only 4 unit cells and resembles a (2×2) superlattice where every second row along [001] is missing. We refrain, here, from the determination of the atomic structure within these three reconstructions which would require a detailed comparison of the STM images to first principles calculations.

Spectra on the Nb(110) substrate show a distinct peak at $V \approx -450$ mV (dashed line in Figure 1f), which has previously been identified as the signature of the d_{z^2} -type surface state of Nb(110),⁴³ providing additional evidence that the Nb substrate is indeed largely clean and free from oxygen. Its spectral signature is still present, yet strongly suppressed,

for the type I Fe ML reconstruction, but it is barely visible as a shoulder for the type II reconstruction and completely suppressed for the type III reconstruction. Instead all Fe ML reconstructions display a peak at $V \approx +400$ mV (dashed line in Figure 1f) which is absent on Nb(110). After the identification of the three types of Fe ML reconstructions grown on the clean Nb(110) we continue with the investigation of their magnetic properties.

Spin orders of the Fe ML reconstructions

To investigate the magnetism of the three types of Fe MLs, spin-resolved scanning tunneling spectroscopy (SP-STs) has been performed. Using a spin-polarized STM tip (see Methods), spectra taken on different regions of the reconstructions for varying out-of-plane magnetic fields within a bias range of $V = \pm 1$ V (Supplementary Note 2 and Figure S2) reveal the particular bias voltages that have been used in the following in order to achieve maximum spin-contrast in spin-resolved dI/dV maps. To emphasize the magnetic contrast over electronic contributions, asymmetry maps were calculated (see Methods, Eq. (1)). Examples of such spin asymmetry maps for $B_{z_{1,2}} = \pm 0.5$ T taken from one of each type of the Fe ML islands shown in Figure 2d can be seen in Figure 2a-c. It is apparent that the type I ML exhibits the strongest spin contrast, followed by type II and type III. For type I, a contrast reversal between flat and stripe regions can be observed, which we will discuss below. Hysteresis loops extracted from out-of-plane magnetic field dependent dI/dV maps (see Methods) by averaging over a certain region on top of each type of Fe ML island are shown in Figure 2e. They reveal a butterfly shaped hysteresis for type I and type II with a strong change in the spin-resolved signal, while there is hardly any change at first sight on the type III Fe ML. Since, for these measurements, only a small amount of magnetic Fe material was transferred onto the Nb tip (see Methods), it is expected that the tip is soft magnetic and aligns parallel to the external magnetic field already at several hundreds of mT.⁴⁴ This is indeed evidenced by the hysteresis loops measured on type I and II islands. After an initial increase in the dI/dV signal for the first few hundreds of mT up to $B_z = \pm 0.5$ T, a contrast

difference relative to $B_z = 0$ T can be seen for all island types I and II, regardless of their size. In contrast, assuming a constant tip magnetization for this magnetic field regime would imply that all islands switch their magnetization at a similar, very small coercive field, which is highly unlikely. We, therefore, conclude that for $|B_z| > 0.5$ T, the tip magnetization points down (up, w.l.o.g.) for negative (positive) magnetic field in Figure 2e. This is also schematically shown in Figure 2f. After this characterization of the tip magnetization, which is the same for the measurements on all three ML types in Figure 2e, we can now interpret the rest of the hysteresis loops, starting with the type I ML (Figure 2e, blue data). For this type, dI/dV values were averaged over flat as well as stripe regions (see Supplementary Note 2 and Figure S2), with only the results over the flat regions shown here. For the downwards sweep (along the direction of the horizontal arrow), the dI/dV signal first increases between $B_z = 0$ T to $B_z = -0.5$ T due to the downwards reorientation of the tip magnetization, and then stays constant until about -2T. Between -2T and -2.4T the dI/dV signal suddenly decreases. When the magnetic field is swept up again, the dI/dV signal first increases between -0.5T and +0.5T due to the upwards reorientation of the tip magnetization, then stays constant up to about +2T, and then suddenly decreases again between +2T and +2.4T. We thus assign the changes in the dI/dV signal between ± 2 T and ± 2.4 T to the change in the magnetization of the type I island (see the sketch in Figure 2f). Exactly the same behaviour of the hysteresis loop is observed on the stripe regions, just with the inverted spin contrast that was already implied by the spin asymmetry map in Figure 2a (see Supplementary Note 2 and Figure S2). We neither observe any indications for non-collinear spin-structures,⁴⁵ nor a shifting in the maximum spin contrast between the stripe and flat regions which would imply unreasonably small domains (Supplementary Note 3 and Figure S3). Therefore, we conclude that this type I reconstruction island has a single-domain out-of-plane ferromagnetic spin-order with a coercive field of $2.2 \text{ T} \pm 0.2 \text{ T}$. The sign-changes in the spin-asymmetry (Figure 2a) are most probably due to an inversion of the vacuum spin-polarization above the stripes with respect to the flat regions (Supplementary Note 2 and Figure S2).⁴⁶

The magnetization curve measured on the type II island (Figure 2e, orange data points) shows qualitatively the same behaviour indicating a single domain out-of-plane ferromagnetic spin order also in this case. However, here the coercive field is considerably smaller ($0.75 \text{ T} \pm 0.25 \text{ T}$). For the magnetization curve measured on the type III island, the dI/dV signal stays largely constant for the entire magnetic field range, apart from some tiny signal changes in the small field regime where the tip magnetization direction is reoriented. This also holds true if we use bias voltages in the entire range between $\pm 1 \text{ V}$ (see Supplementary Note 2 and Figure S2). This result can lead to one of the three following implications: Firstly, the magnetization of the type III Fe ML reconstruction could be quenched. This can be excluded due to the residual spin contrast in the low magnetic field range and since this type of ML induces Shiba states in the band gap of the superconducting substrate (see below). Secondly, while the tip's magnetization is out-of-plane for $|B_z| > 0.5 \text{ T}$, a strong in-plane magnetic anisotropy could force the Fe spins in the type III ML islands into the direction perpendicular to the tip magnetization, thus yielding zero spin contrast. This scenario can be excluded by Monte-Carlo simulations (see Supplementary Note 4 and Figure S4) showing that, even for relatively strong in-plane magnetic anisotropies of a ferromagnetic island, the maximum magnetic field would still yield an out-of-plane magnetization of 25% of the saturation magnetization which could be experimentally detected,⁴⁷ in conflict with the measurements. Therefore, the most likely scenario would be that the type III ML has a very low coercivity of $< 0.4 \text{ T}$ which is comparable to that of the tip.

In order to check the general validity of the above results for the different types of Fe ML islands, we investigated several islands of each type also using different tips (see Supplementary Note 5 and Table 1). They show, that the coercive fields do not vary considerably with island sizes or shapes, but are largely determined by the type of the reconstruction, i.e. dipolar interaction effects seem negligible. This can be rationalized by our Monte-Carlo simulations (see Supplementary Note 4 and Figure S4).^{48,49} While this model simulates the very simplified situation of a ferromagnetic island with homogeneous properties, instead

of a strongly reconstructed island where the magnetic properties will change from site to site, it still enables to understand the general trends by mapping the lateral changes in the magnetism in the different reconstructions to site-independent magnetic moments, onsite magnetic anisotropies and nearest neighbor Heisenberg exchange interactions. While we assume that the magnetic moment of the Fe atoms in the three types of MLs are similar ($\mu = 2.5\mu_B$), we vary the magnetic anisotropy constants ($K_z, K_x = -0.05 \dots -0.5$ meV) and exchange constant ($J_1 = 1 \dots 5$ meV per bond) within reasonable constraints. These simulations reveal that islands of the investigated sizes reverse their magnetization by domain wall nucleation and propagation. The simulated coercive field is largely proportional to the square root of the product of anisotropy and exchange constants and can reproduce the measured coercive fields. Considering the differences in the coercive fields (2.3 T for type I, 0.7 T for type II, and < 0.4 T for type III) we conclude that the overall anisotropy times exchange constants for the Fe atoms in the islands are decreasing by orders of magnitude with a ratio of $5.3/0.49/ < 0.16$ going from type I, over type II, to type III ML. There might be, of course, additional effects of the different structural disorder of the three types of reconstructions on the coercive field via inducing nucleation centers for the domain walls. In the following, we will investigate the local properties of the Shiba bands which are expected to form by hybridization of the Yu-Shiba-Rusinov states of the Fe atoms in the islands,³⁻⁵ and how they differ for the three types of MLs due to their different structural and spin-dependent properties.

Disordered Shiba bands in the reconstructed Fe MLs

Spectroscopic line profiles taken with a superconducting tip from the Nb substrate across one of each type of the Fe ML islands are shown in Figure 3a-c and the averaged spectra of those line profiles on top of the Fe MLs and on Nb are shown in Figure 3d. Since the tip has an energy gap of $\Delta_t = 1.00$ meV, the energies of all observed features are shifted by 1 meV relative to the Fermi energy E_F (Methods). As we are interested in the states induced by the

Fe islands in the gap of the substrate, we focus on the energy range from $\pm\Delta_t = \pm 1$ meV to $\pm(\Delta_s + \Delta_t) = \pm 2.40$ meV. While the substrate coherence peaks at $\pm(\Delta_s + \Delta_t)$ are strongly suppressed on top of all islands, there is an increase in spectral intensity all over the gap region compared to the Nb substrate. We assign this spectral intensity to the Shiba bands, which should form by hybridization of the Yu-Shiba-Rusinov states of the individual Fe atoms in the islands.³⁻⁵ Comparing the three types of MLs, there are pronounced differences in the overall intensities of the Shiba bands and their lateral variations which we will investigate in the following. While the coherence peak is increasingly suppressed going from the low coercivity type III over type II to the high coercivity type I islands, the energy-averaged intensity of the Shiba bands behaves opposite, i.e. it increases. This is also apparent from two-dimensional maps over an area with several islands (see Figure 4a) of the spectral weight at E_F (Figure 4b) and at the coherence peak (Figure 4c), respectively. Importantly, for all three ML types, the Shiba bands have significant intensities close to E_F , suggesting that their band widths are large enough to overlap with E_F . But there is no indication of a gap opening at E_F (Figure 3). However, this behaviour is complicated by a strong lateral variation in the spectral weight of the Shiba bands revealing shifts on the order of the substrate gap energy, which also differs between the three island types. The lateral variation is weakest for the type III ML and most pronounced for type I, and seems to have a correlation length comparable to the periodicity of the respective reconstruction. We assign these lateral variations to disorder in the Shiba bands induced by the strong structural disorder of the different Fe ML reconstructions. For the type I islands, a very strong and long range variation reveals nm sized areas on top of the islands with an intense spectral weight at $\pm\Delta_t$ (see vertical white line on the center of the island in the spectral line profile of Figure 3a), i.e. close to E_F , which are also visible in Figure 4b. These special features occur only in sufficiently wide flat areas between the stripes when they have a minimum spacing of 3 nm (see white dot in the center of the island marked on the red line on the STM image of Figure 3a). However, note that the particle-hole asymmetry in the intensities of these features indicates, that they are

not related to a zero energy state, but probably to a trivial state which is bound close to E_F and localized by the disorder potential in the Shiba bands. Besides these different strengths of the disorder potentials in the Shiba bands for the three Fe ML reconstructions, the other main result of the current work is, that for all three types of ferromagnetic Fe MLs, there are no clear indications for any edge states, in the entire energy region of the substrate gap. Such edge states would be observed in the left and right regions of the spectral line profiles in Figure 3a-c between the vertical white lines marking the edges of the islands. In particular, there are no indications for any zero energy edge modes as can be seen in Figure 4b. As a side remark, we mention here, that the islands display a negligible inverse proximity effect on the Nb(110) substrate, which can be seen by the immediate recovery of the coherence peak spectral intensity in less than a nm distance to all islands edges (Figure 4c,d), unlike it was observed for other systems.²⁰

Conclusions

In conclusion, our study unravels a correlation between different types of reconstruction-induced structural disorder in ferromagnetic Fe ML islands on clean Nb(110) with their coercive magnetic fields as well as with the spectral intensity and disorder in the Shiba bands which they induce in the superconductor. We assign the effect of the difference in reconstruction on the coercive field to a change in the magnetic anisotropy and/or exchange constant between the three different ML types. The different magnetic couplings in cooperation with the different types of structural disorder in the three ferromagnetic spin-lattices naturally explain a different disorder potential of their Shiba bands. The latter is quite massive, i.e. on the order of the superconducting energy gap for the spin-lattice with the strongest anisotropy times exchange constants and longest correlation length of the reconstruction, i.e. type I. Notably, the energetic position of YSR states has proven to be quite sensitive to disorder in previous studies, e.g. crucially depends on the exact adsorption site,⁵⁰ on the position relative to oxygen impurities^{51,52} or on the position relative to the charge density wave

in NbSe₂.⁵³ The increasing spectral intensity in the Shiba bands for increasing anisotropy times exchange constants in the spin lattice naively seems intuitive, as in the classical model of Yu-Shiba-Rusinov, an increase in the magnetic moment or exchange interaction to the conduction electrons of the superconductor usually induces a shift of the Yu-Shiba-Rusinov states of individual atoms from the coherence peak into the gap region.^{50,54} However, as this shift continues, the spectral weight will move towards the coherence peaks on the other side of E_F , which would probably balance the former effect. In the spin-lattice, in addition to these effects, an increasing exchange coupling between Yu-Shiba-Rusinov states will widen the Shiba bands,²³ and this exchange coupling most probably is also different for the three ML types as it might be linked to the one that determines the coercivity. Most importantly, our study reveals that there are neither indications for a gap at E_F , nor of any edge states for all three types of disordered ferromagnetic spin-lattices investigated here, neither at nor off the Fermi energy. Naively thinking, the system might fulfill all requirements for topological superconductivity, i.e. a ferromagnetic spin-lattice which realizes Shiba bands that are overlapping with E_F and very likely have a considerable spin-orbit interaction.⁵⁵ However, as shown in previous publications on 1D systems, the formation of topological edge modes can be hindered by the interaction of multiple Shiba bands originating from the five 3d orbitals of the Fe lattice.^{56,57} Additionally, in the reconstructed ML system investigated here, we have experimentally proven a substantial disorder in the Shiba bands which can have both, a potential and a magnetic origin. As outlined in the introduction, excluding very specific and rare values of the chemical potential or specific types of disorder,^{17,35,38} the strong disorder on the order of the pairing energy present in the investigated lattices would destroy any topological gap as well as topological edge modes.^{33,35,36} We, therefore, conclude that besides a specific design of the multi-orbital Shiba bands in ferromagnetic layers in direct contact to elemental superconductors,²³ a pseudomorphic growth with the least amount of disorder is probably best suited for the design of two-dimensional topological superconductivity and the related Majorana edge modes. This yet adds another constraint and further narrows down

the number of experimental systems which are suitable for the realization of this intriguing quantum state.

Methods

All measurements were obtained in two low-temperature ultra-high vacuum STM facilities, one is a home-built system operating at 6.5 K,⁵⁸ and the other is a commercially available system with home-built UHV chambers operating at 4.5 K.⁵⁹ The Nb(110) crystal was cleaned by several cycles of Ar⁺ sputtering and high-temperature annealing using an electron beam heater at a power of at least 510 W (see Supplementary Note 1), following the recipe described by Odobesko et al.⁴³ Immediately after the cleaning, 0.52 ML Fe was deposited *in-situ* from an e-beam evaporator at a rate of about one ML per minute onto the Nb(110) substrate held at room temperature (RT). STM-images were taken at constant tunnel current I with a bias voltage V applied to the sample, for which the corresponding values are given in the figure captions. dI/dV point spectra were obtained by stabilizing the tip at a given point above the surface at stabilization current $I_{\text{stab}} = 500$ pA and bias $V_{\text{stab}} = 1$ V, switching off the feedback loop, and recording the differential tunneling conductance as a function of sample bias V using standard Lock-In technique where the modulation voltage $V_{\text{mod}} = 10$ mV of frequency $f = 1.197$ kHz is added to the bias voltage. Spectroscopic line profiles and spectroscopic fields were taken by recording point spectra on one- and two-dimensional grids, respectively, over the surface. In contrast, dI/dV maps were recorded in constant-current mode in parallel to usual STM-images.

For the atomically resolved STM-images (Figure 1, $T = 6.5$ K) an electrochemically etched tungsten tip was used. For the SP-STs measurements (Figure 2, $T = 4.5$ K), a mechanically sharpened Nb bulk tip was gently dipped into an Fe island in order to obtain a spin-polarized tip. After dipping, point spectroscopy on Nb(110) was performed to check for the presence of sub-gap states within the tip's superconducting gap, which indicate that magnetic material

has been successfully transferred to the tip.^{60–62} To emphasize the spin-resolved contrast, which is not easily seen in the individual dI/dV maps $(dI/dV)_{ij}^{B_{z_1}}$ or $(dI/dV)_{ij}^{B_{z_2}}$ taken at various magnetic fields B_{z_1} and B_{z_2} , respectively, spin asymmetry maps were calculated by

$$\text{asym}_{ij} = \frac{(dI/dV)_{ij}^{B_{z_1}} - (dI/dV)_{ij}^{B_{z_2}}}{(dI/dV)_{ij}^{B_{z_1}} + (dI/dV)_{ij}^{B_{z_2}}}. \quad (1)$$

Furthermore, for the plot of the hysteresis loops in Fig 2 e, dI/dV maps were taken for different out-of-plane applied magnetic fields varied in a loop sequence, as indicated. The dI/dV values were normalized and averaged over a selected area of the different Fe island types and then plotted versus the external B_z values. All other spin-averaged measurements (Figures 3 and 4, $T = 4.5$ K) were performed with a pure Nb bulk tip, which increases the energy resolution at elevated temperatures beyond the Fermi-Dirac limit.^{63,64} Therefore, the corresponding dI/dV values reflecting features in the sample LDOS are shifted by the energy of the tip gap Δ_t . The latter can be determined for each tip by taking a point spectrum on the substrate, see Figure 3d. The peaks of largest intensity appear at $e \cdot V = \pm(\Delta_s - \Delta_t) = \pm 0.38$ meV and $\pm(\Delta_s + \Delta_t) = \pm 2.38$ meV. Thereby, we get the corresponding energy gaps of $\Delta_t = 1.00$ meV and $\Delta_s = 1.38$ meV (at $T = 4.5$ K).

Acknowledgement

We thank Elena Y. Vedmedenko, Maciej Bazarnik, Eric Mascot as well as Roberto Lo Conte for fruitful discussions. J.J.G. and R.W. gratefully acknowledge funding by the European Union via the ERC Advanced Grant ADMIRE (No. 786020). L.S., D.W., J.W. and R.W. acknowledge funding by the Cluster of Excellence ‘Advanced Imaging of Matter’ (EXC 2056—project ID 390715994) of the Deutsche Forschungsgemeinschaft (DFG). K.T.T., Y.M., J.W. and R.W. acknowledge funding by the Deutsche Forschungsgemeinschaft (DFG, German Research Foundation) – SFB-925 – project 170620586.

References

- (1) Qi, X.-L.; Hughes, T. L.; Zhang, S.-C. Chiral topological superconductor from the quantum Hall state. *Phys. Rev. B* **2010**, *82*, 184516.
- (2) Kitaev, A. Fault-tolerant quantum computation by anyons. *Annals of Physics* **2003**, *303*, 2–30.
- (3) Röntynen, J.; Ojanen, T. Topological Superconductivity and High Chern Numbers in 2D Ferromagnetic Shiba Lattices. *Phys. Rev. Lett.* **2015**, *114*, 236803.
- (4) Röntynen, J.; Ojanen, T. Chern mosaic: Topology of chiral superconductivity on ferromagnetic adatom lattices. *Phys. Rev. B* **2016**, *93*, 094521.
- (5) Li, J.; Neupert, T.; Wang, Z.; Macdonald, A. H.; Yazdani, A.; Bernevig, B. A. Two-dimensional chiral topological superconductivity in Shiba lattices. *Nature Communications* **2016**, *7*, 1–7.
- (6) Rachel, S.; Mascot, E.; Cocklin, S.; Vojta, M.; Morr, D. K. Quantized charge transport in chiral Majorana edge modes. *Phys. Rev. B* **2017**, *96*, 205131.
- (7) Zlotnikov, A. O.; Shustin, M. S.; Fedoseev, A. D. Aspects of Topological Superconductivity in 2D Systems: Noncollinear Magnetism, Skyrmions, and Higher-order Topology. *Journal of Superconductivity and Novel Magnetism* **2021**, *34*, 3053–3088.
- (8) Nakosai, S.; Tanaka, Y.; Nagaosa, N. Two-dimensional p -wave superconducting states with magnetic moments on a conventional s -wave superconductor. *Phys. Rev. B* **2013**, *88*, 180503.
- (9) Chen, W.; Schnyder, A. P. Majorana edge states in superconductor-noncollinear magnet interfaces. *Phys. Rev. B* **2015**, *92*, 214502.
- (10) Pershoguba, S. S.; Nakosai, S.; Balatsky, A. V. Skyrmion-induced bound states in a superconductor. *Phys. Rev. B* **2016**, *94*, 064513.

- (11) Yang, G.; Stano, P.; Klinovaja, J.; Loss, D. Majorana bound states in magnetic skyrmions. *Phys. Rev. B* **2016**, *93*, 224505.
- (12) Mohanta, N.; Okamoto, S.; Dagotto, E. Skyrmion control of Majorana states in planar Josephson junctions. *Communications Physics* **2021**, *4*, 163.
- (13) Mascot, E.; Bedow, J.; Graham, M.; Rachel, S.; Morr, D. K. Topological superconductivity in skyrmion lattices. *npj Quantum Materials* **2021**, *6*, 6.
- (14) Garnier, M.; Mesaros, A.; Simon, P. Topological superconductivity with deformable magnetic skyrmions. *Communications Physics* **2019**, *2*, 126.
- (15) Palacio-Morales, A.; Mascot, E.; Cocklin, S.; Kim, H.; Rachel, S.; Morr, D. K.; Wiesendanger, R. Atomic-scale interface engineering of Majorana edge modes in a 2D magnet-superconductor hybrid system. *Science Advances* **2019**, *5*, eaav6600.
- (16) Kezilebieke, S.; Huda, M. N.; Vaňo, V.; Aapro, M.; Ganguli, S. C.; Silveira, O. J.; Głodzik, S.; Foster, A. S.; Ojanen, T.; Liljeroth, P. Topological superconductivity in a van der Waals heterostructure. *Nature* **2020**, *588*, 424–428.
- (17) Kezilebieke, S.; Vaňo, V.; Huda, M. N.; Aapro, M.; Ganguli, S. C.; Liljeroth, P.; Lado, J. L. Moiré-Enabled Topological Superconductivity. *Nano Letters* **2022**, *22*, 328–333, PMID: 34978831.
- (18) Ménard, G. C.; Guissart, S.; Brun, C.; Leriche, R. T.; Trif, M.; Debontridder, F.; Demaille, D.; Roditchev, D.; Simon, P.; Cren, T. Two-dimensional topological superconductivity in Pb/Co/Si(111). *Nature Communications* **2017**, *8*, 2040.
- (19) Ménard, G. C.; Mesaros, A.; Brun, C.; Debontridder, F.; Roditchev, D.; Simon, P.; Cren, T. Isolated pairs of Majorana zero modes in a disordered superconducting lead monolayer. *Nature Communications* **2019**, *10*, 2587.

- (20) Mougel, L.; Buhl, P. M.; Li, Q.; Müller, A.; Yang, H.-H.; Verstraete, M.; Simon, P.; Dupé, B.; Wulfskel, W. The role of band matching in the proximity effect between a superconductor and a normal metal. *arXiv:2203.01393* **2022**,
- (21) Lo Conte, R.; Bazarnik, M.; Palotás, K.; Rózsa, L.; Szunyogh, L.; Kubetzka, A.; von Bergmann, K.; Wiesendanger, R. Coexistence of Antiferromagnetism and Superconductivity in Mn/Nb(110). *Phys. Rev. B* **2022**, *105*, L100406.
- (22) Wang, Z.; Rodriguez, J. O.; Jiao, L.; Howard, S.; Graham, M.; Gu, G. D.; Hughes, T. L.; Morr, D. K.; Madhavan, V. Evidence for dispersing 1D Majorana channels in an iron-based superconductor. *Science* **2020**, *367*, 104–108.
- (23) Schneider, L.; Beck, P.; Neuhaus-Steinmetz, J.; Rózsa, L.; Posske, T.; Wiebe, J.; Wiesendanger, R. Precursors of Majorana modes and their length-dependent energy oscillations probed at both ends of atomic Shiba chains. *Nature Nanotechnology* **2022**, *17*, 384–389.
- (24) Küster, F.; Brinker, S.; Lounis, S.; Parkin, S. S. P.; Sessi, P. Long range and highly tunable interaction between local spins coupled to a superconducting condensate. *Nature Communications* **2021**, *12*, 6722.
- (25) Mascot, E.; Cocklin, S.; Rachel, S.; Morr, D. K. Dimensional tuning of Majorana fermions and real space counting of the Chern number. *Phys. Rev. B* **2019**, *100*, 184510.
- (26) Buzdin, A. I. Proximity effects in superconductor-ferromagnet heterostructures. *Rev. Mod. Phys.* **2005**, *77*, 935–976.
- (27) Bergeret, F. S.; Volkov, A. F.; Efetov, K. B. Odd triplet superconductivity and related phenomena in superconductor-ferromagnet structures. *Rev. Mod. Phys.* **2005**, *77*, 1321–1373.

- (28) Linder, J.; Yokoyama, T.; Sudbø, A. Theory of superconducting and magnetic proximity effect in S/F structures with inhomogeneous magnetization textures and spin-active interfaces. *Phys. Rev. B* **2009**, *79*, 054523.
- (29) Mühge, T.; Theis-Bröhl, K.; Westerholt, K.; Zabel, H.; Garif'yanov, N. N.; Goryunov, Y. V.; Garifullin, I. A.; Khaliullin, G. G. Influence of magnetism on superconductivity in epitaxial Fe/Nb bilayer systems. *Phys. Rev. B* **1998**, *57*, 5071–5074.
- (30) Mühge, T.; Goryunov, Y. V.; Theis-Bröhl, K.; Westerholt, K.; Zabel, H.; Garifullin, I. A. Proximity effect in superconductor/ferromagnet layered system: Influence of superconductivity on magnetic properties of Nb/Fe epitaxial bilayers. *Applied Magnetic Resonance* **1998**, *14*, 567–582.
- (31) Kim, Y.; Cheng, M.; Bauer, B.; Lutchyn, R. M.; Das Sarma, S. Helical order in one-dimensional magnetic atom chains and possible emergence of Majorana bound states. *Phys. Rev. B* **2014**, *90*, 060401.
- (32) Hui, H.-Y.; Sau, J. D.; Das Sarma, S. Bulk disorder in the superconductor affects proximity-induced topological superconductivity. *Phys. Rev. B* **2015**, *92*, 174512.
- (33) Westström, A.; Pöyhönen, K.; Ojanen, T. Topological superconductivity and anti-Shiba states in disordered chains of magnetic adatoms. *Phys. Rev. B* **2016**, *94*, 104519.
- (34) Awoga, O. A.; Björnson, K.; Black-Schaffer, A. M. Disorder robustness and protection of Majorana bound states in ferromagnetic chains on conventional superconductors. *Phys. Rev. B* **2017**, *95*, 184511.
- (35) Mascot, E.; Agrahar, C.; Rachel, S.; Morr, D. K. Stability of disordered topological superconducting phases in magnet-superconductor hybrid systems. *Phys. Rev. B* **2019**, *100*, 235102.

- (36) Lu, Y.; Virtanen, P.; Heikkilä, T. T. Effect of disorder on Majorana localization in topological superconductors: A quasiclassical approach. *Phys. Rev. B* **2020**, *102*, 224510.
- (37) Christian, C.; Dumitrescu, E. F.; Halász, G. B. Robustness of vortex-bound Majorana zero modes against correlated disorder. *Phys. Rev. B* **2021**, *104*, L020505.
- (38) Pöyhönen, K.; Sahlberg, I.; Westström, A.; Ojanen, T. Amorphous topological superconductivity in a Shiba glass. *Nature Communications* **2018**, *9*, 2103.
- (39) Kamlapure, A.; Cornils, L.; Wiebe, J.; Wiesendanger, R. Engineering the spin couplings in atomically crafted spin chains on an elemental superconductor. *Nature Communications* **2018**, *9*, 3253.
- (40) Liebhaber, E.; Rütten, L. M.; Reecht, G.; Steiner, J. F.; Rohlf, S.; Rossnagel, K.; von Oppen, F.; Franke, K. J. Quantum spins and hybridization in artificially-constructed chains of magnetic adatoms on a superconductor. *Nature Communications* **2021**, *13*, 2160.
- (41) Mougín, A.; Andrieu, S.; Dufour, C.; Dumesnil, K. Epitaxial growth of Fe on Nb(110). *Surface Science* **2002**, *518*, 175–182.
- (42) Wolf, C.; Köhler, U. Growth and intermixing of Nb on Fe(110) and Fe on Nb(110). *Thin Solid Films* **2006**, *500*, 347–355.
- (43) Odobesko, A. B.; Haldar, S.; Wilfert, S.; Hagen, J.; Jung, J.; Schmidt, N.; Sessi, P.; Vogt, M.; Heinze, S.; Bode, M. Preparation and electronic properties of clean superconducting Nb(110) surfaces. *Phys. Rev. B* **2019**, *99*, 115437.
- (44) Wiebe, J.; Zhou, L.; Wiesendanger, R. Atomic magnetism revealed by spin-resolved scanning tunnelling spectroscopy. *Journal of Physics D: Applied Physics* **2011**, *44*, 464009.

- (45) Bode, M.; Heide, M.; von Bergmann, K.; Ferriani, P.; Heinze, S.; Bihlmayer, G.; Kubetzka, A.; Pietzsch, O.; Blügel, S.; Wiesendanger, R. Chiral magnetic order at surfaces driven by inversion asymmetry. *Nature* **2007**, *447*, 190–193.
- (46) Zhou, L.; Meier, F.; Wiebe, J.; Wiesendanger, R. Inversion of spin polarization above individual magnetic adatoms. *Phys. Rev. B* **2010**, *82*, 012409.
- (47) Doi, K.; Minamitani, E.; Yamamoto, S.; Arafune, R.; Yoshida, Y.; Watanabe, S.; Hasegawa, Y. Electronic and magnetic effects of a stacking fault in cobalt nanoscale islands on the Ag(111) surface. *Phys. Rev. B* **2015**, *92*, 064421.
- (48) Hagemester, J.; Iaia, D.; Vedmedenko, E. Y.; von Bergmann, K.; Kubetzka, A.; Wiesendanger, R. Skyrmions at the Edge: Confinement Effects in Fe/Ir(111). *Phys. Rev. Lett.* **2016**, *117*, 207202.
- (49) Hagemester, J. MONTECRYSTAL. <https://github.com/JHagemester/MonteCrystal>, accessed 2020-01-12.
- (50) Schneider, L.; Steinbrecher, M.; Rózsa, L.; Bouaziz, J.; Palotás, K.; dos Santos Dias, M.; Lounis, S.; Wiebe, J.; Wiesendanger, R. Magnetism and in-gap states of 3d transition metal atoms on superconducting Re. *npj Quantum Materials* **2019**, *4*, 42.
- (51) Odobesko, A.; Di Sante, D.; Kowalski, A.; Wilfert, S.; Friedrich, F.; Thomale, R.; Sangiovanni, G.; Bode, M. Observation of tunable single-atom Yu-Shiba-Rusinov states. *Physical Review B* **2020**, *102*, 174504.
- (52) Friedrich, F.; Boshuis, R.; Bode, M.; Odobesko, A. Coupling of Yu-Shiba-Rusinov states in one-dimensional chains of Fe atoms on Nb(110). *Phys. Rev. B* **2021**, *103*, 235437.
- (53) Liebhaber, E.; Acero González, S.; Baba, R.; Reecht, G.; Heinrich, B. W.; Rohlf, S.; Rossnagel, K.; von Oppen, F.; Franke, K. J. Yu–Shiba–Rusinov States in the Charge-

- Density Modulated Superconductor NbSe₂. *Nano Letters* **2020**, *20*, 339–344, PMID: 31842547.
- (54) Küster, F.; Montero, A. M.; Guimarães, F. S. M.; Brinker, S.; Lounis, S.; Parkin, S. S. P.; Sessi, P. Correlating Josephson supercurrents and Shiba states in quantum spins unconventionally coupled to superconductors. *Nature Communications* **2021**, *12*, 1108.
- (55) Beck, P.; Schneider, L.; Rózsa, L.; Palotás, K.; Lászlóffy, A.; Szunyogh, L.; Wiebe, J.; Wiesendanger, R. Spin-orbit coupling induced splitting of Yu-Shiba-Rusinov states in antiferromagnetic dimers. *Nature Communications* **2021**, *12*, 2040.
- (56) Schneider, L.; Beck, P.; Posske, T.; Crawford, D.; Mascot, E.; Rachel, S.; Wiesendanger, R.; Wiebe, J. Topological Shiba bands in artificial spin chains on superconductors. *Nature Physics* **2021**, *17*, 943–948.
- (57) Küster, F.; Brinker, S.; Hess, R.; Loss, D.; Parkin, S.; Klinovaja, J.; Lounis, S.; Sessi, P. Non-Majorana modes in diluted spin chains proximitized to a superconductor. 2021; <https://arxiv.org/abs/2112.05708>.
- (58) Wittneven, C.; Dombrowski, R.; Pan, S. H.; Wiesendanger, R. A low-temperature ultrahigh-vacuum scanning tunneling microscope with rotatable magnetic field. *Review of Scientific Instruments* **1997**, *68*, 3806–3810.
- (59) Löptien, P.; Zhou, L.; Khajetoorians, A. A.; Wiebe, J.; Wiesendanger, R. Superconductivity of lanthanum revisited: enhanced critical temperature in the clean limit. *Journal of Physics: Condensed Matter* **2014**, *26*, 425703.
- (60) Huang, H.; Padurariu, C.; Senkpiel, J.; Drost, R.; Yeyati, A. L.; Cuevas, J. C.; Kubala, B.; Ankerhold, J.; Kern, K.; Ast, C. R. Tunnelling dynamics between superconducting bound states at the atomic limit. *Nature Physics* **2020**, *16*, 1227–1231.

- (61) Schneider, L.; Beck, P.; Wiebe, J.; Wiesendanger, R. Atomic-scale spin-polarization maps using functionalized superconducting probes. *Science Advances* **2021**, *7*, eabd7302.
- (62) Huang, H.; Senkpiel, J.; Padurariu, C.; Drost, R.; Villas, A.; Klees, R. L.; Yeyati, A. L.; Cuevas, J. C.; Kubala, B.; Ankerhold, J.; Kern, K.; Ast, C. R. Spin-dependent tunneling between individual superconducting bound states. *Phys. Rev. Research* **2021**, *3*, L032008.
- (63) Pan, S. H.; Hudson, E. W.; Davis, J. C. Vacuum tunneling of superconducting quasiparticles from atomically sharp scanning tunneling microscope tips. *Applied Physics Letters* **1998**, *73*, 2992–2994.
- (64) Ruby, M.; Heinrich, B. W.; Pascual, J. I.; Franke, K. J. Experimental Demonstration of a Two-Band Superconducting State for Lead Using Scanning Tunneling Spectroscopy. *Phys. Rev. Lett.* **2015**, *114*, 157001.

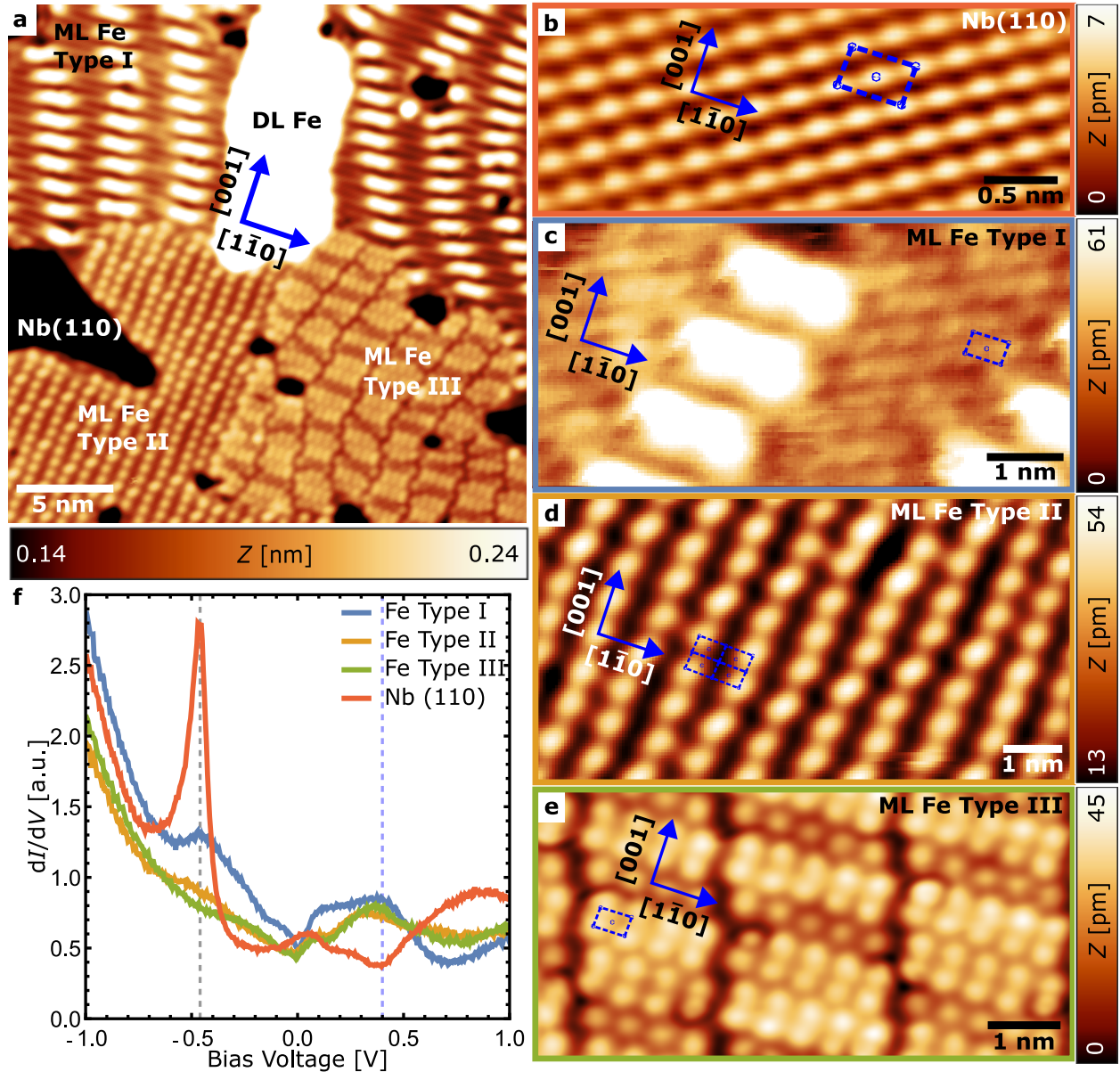


Figure 1: (a) STM image of ML Fe islands having the three distinct reconstructions I, II, III ($V = -10$ mV, $I = 4$ nA, $T = 6.5$ K). Furthermore, a DL Fe island can be identified as a bright stripe. (b)-(e) Atomically resolved STM images of (b) the Nb(110) substrate and (c-e) of the individual Fe ML reconstructions ($T = 6.5$ K; b: $V = -10$ mV, $I = 5$ nA; c: $V = -10$ mV, $I = 5$ nA; d: $V = -10$ mV, $I = 7$ nA; e: $V = -5$ mV, $I = 100$ nA). (f) Point spectra taken on the substrate and the respective Fe ML reconstructions as indicated. Vertical blue dashed lines mark the Nb(110) surface state at negative bias and a state of the Fe ML at positive bias ($V_{\text{stab}} = 1$ V, $V_{\text{mod}} = 10$ mV, $I_{\text{stab}} = 0.5$ nA, $T = 4.5$ K).

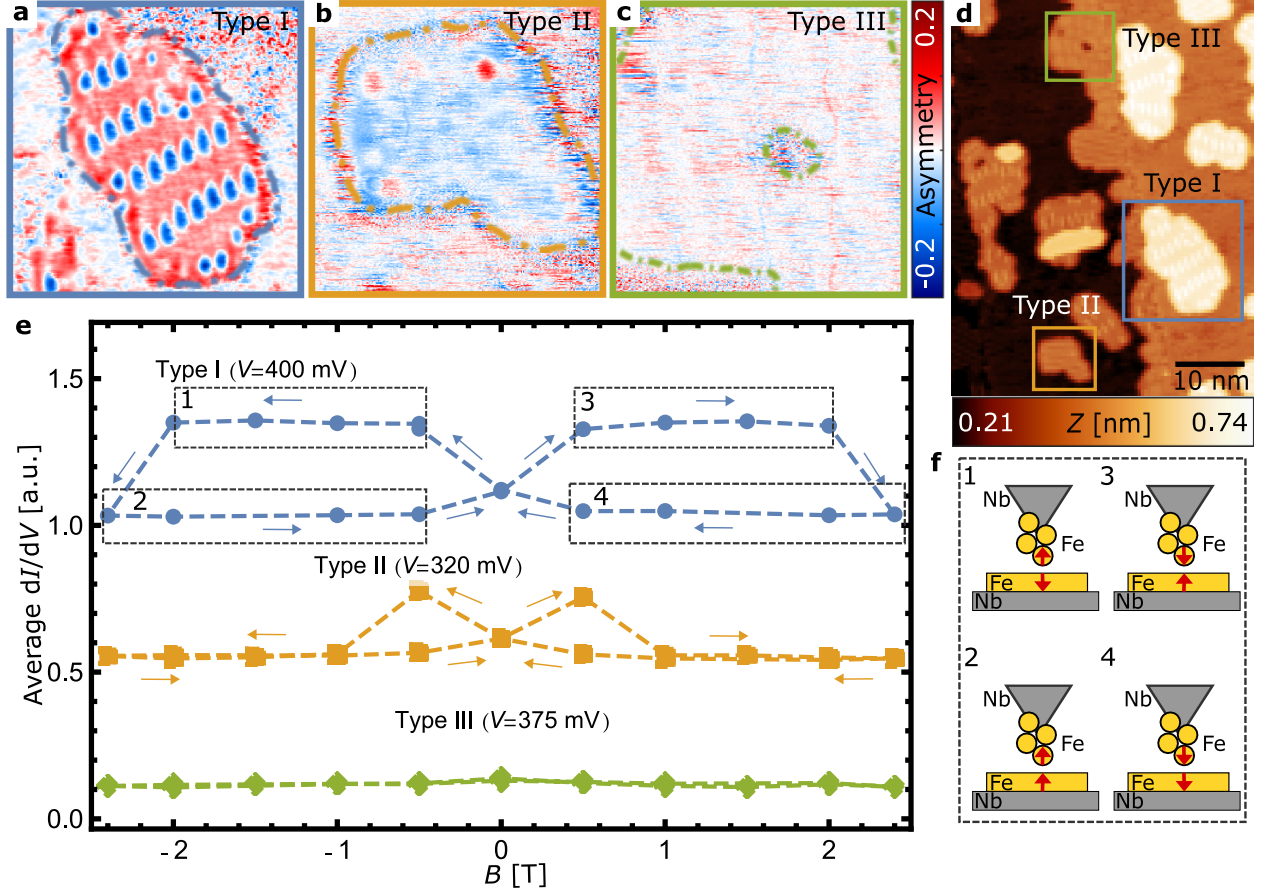


Figure 2: (a)-(c) Spin asymmetry maps ($B_{z_1} = -0.5$ T, $B_{z_2} = +0.5$ T) of the different types of Fe ML reconstructions shown in the STM-image in (d) taken with the same spin-polarized STM tip ($I = 1$ nA, $V_{\text{mod}} = 50$ mV, $V = 400$ mV (a), $V = 320$ mV (b), $V = 375$ mV (c)). The outline of the individual islands is marked using dashed lines with a color according to the code. (e) Hysteresis loops of the same three islands, calculated from spin-resolved dI/dV values at the indicated bias voltages averaged over selected areas of each of the different Fe ML reconstructions. (f) Exemplary sketch of the determined magnetizations of the tip and type I Fe ML island for different parts of the hysteresis loop as indicated by the according numbers in (e). Note, that the magnetic field dependence of the tip magnetization is the same for all three hysteresis loops.

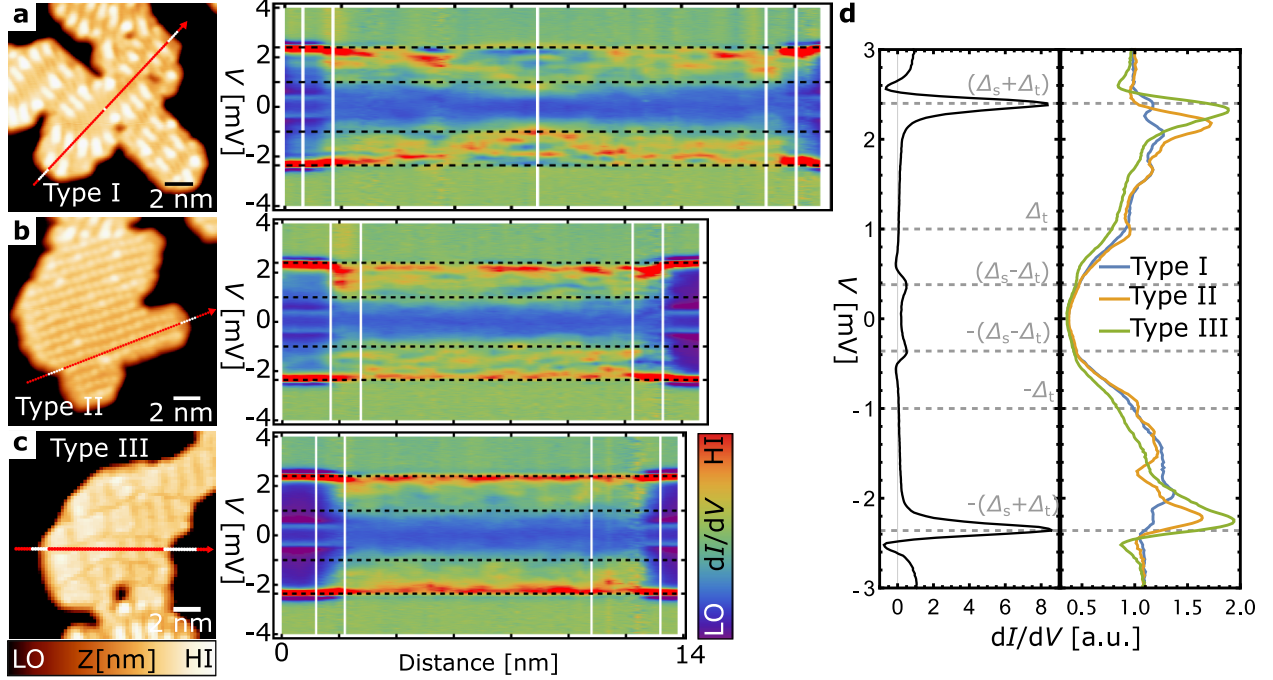


Figure 3: (a)-(c) Left panels are STM-images of three Fe ML islands of each type of reconstruction as indicated ($I = 1$ nA, $V = -6$ mV, $T = 4.5$ K). Right panels are spectroscopic line profiles across each of the island types along the lines in the direction of the arrows ($I_{\text{stab}} = 400$ pA, $V_{\text{mod}} = 0.1$ mV, $V_{\text{stab}} = 4$ mV). The white dots on the arrows in the STM-images correspond to the positions where the spectra inbetween the white vertical lines of the spectroscopic line profiles have been taken. (d) Right panel: Spectra averaged on top of the three islands from the spectroscopic line profiles in (a) to (c). Left panel: Spectrum averaged on an area of the bare Nb(110) surface. Gray or black dashed horizontal lines in the spectra are at $e \cdot V = \pm(\Delta_t - \Delta_s)$, $e \cdot V = \pm\Delta_t$ and $e \cdot V = \pm(\Delta_t + \Delta_s)$.

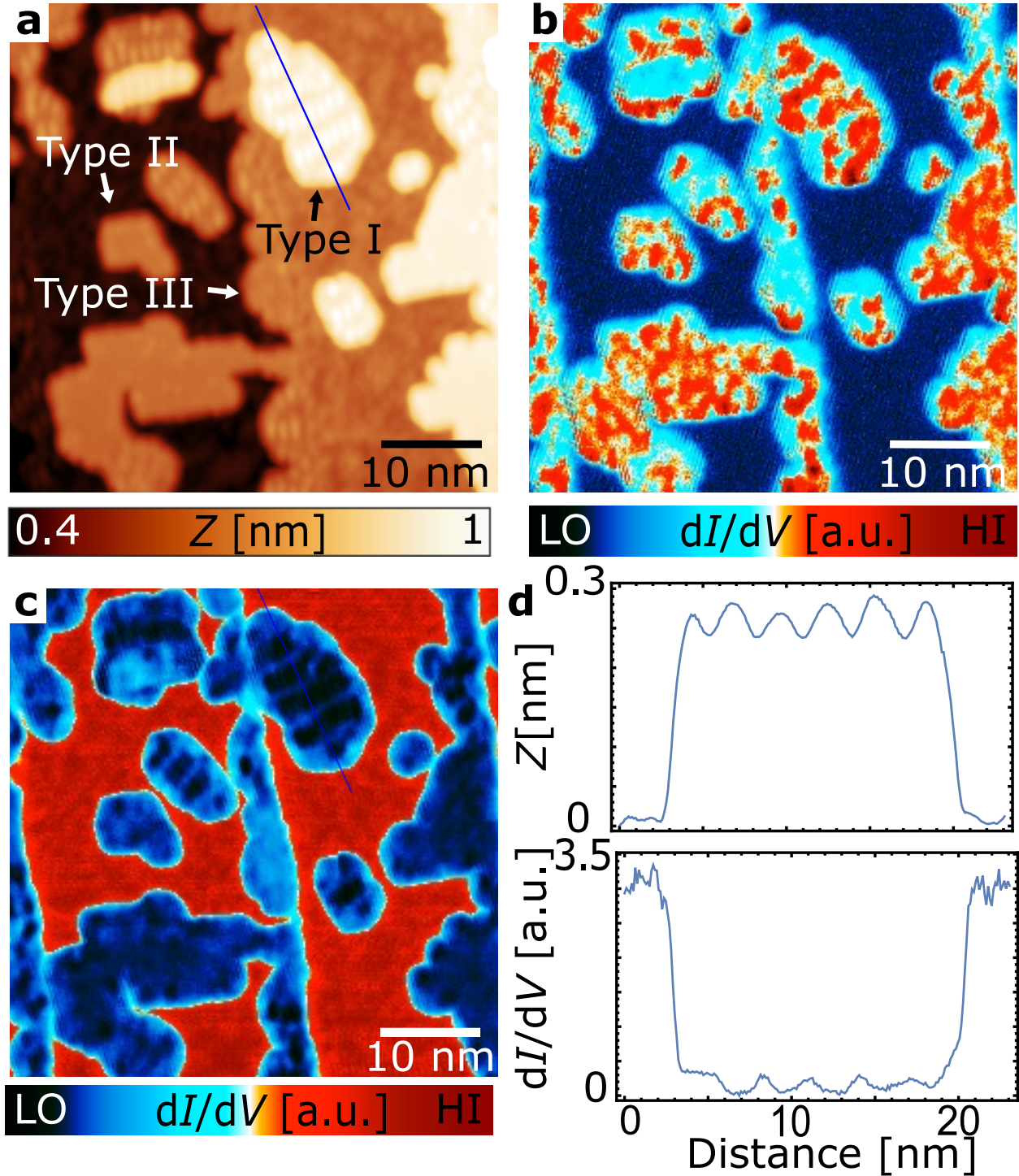


Figure 4: (a) Overview STM image of an area with several Fe ML islands of all three types including some of the islands investigated in Figure 2a-d. (b) Fermi energy and (c) Nb(110) coherence peak spectral weights, respectively, taken from spectroscopic grids over the same area recorded by following the tip height from (a) but with $e \cdot V = 1 \text{ meV} = \Delta_t$ (b) and $e \cdot V = 2.5 \text{ meV} = \Delta_t + \Delta_s$ (c). (d) Line profiles of the height (top panel) and Nb(110) coherence peak spectral weight (bottom) taken along identical lines across the type I island shown in (a) and (c), respectively. ($I = 200 \text{ pA}$, $V = 6 \text{ mV}$, $V_{\text{mod}} = 0.1 \text{ mV}$ (a); $V = 1.13 \text{ mV}$, $V_{\text{mod}} = 0.1 \text{ mV}$ (b); $V = 2.5 \text{ mV}$, $V_{\text{mod}} = 0.1 \text{ mV}$ (c)).